Journal of the Meteorological Society of Japan

EARLY ONLINE RELEASE

The DOI for this manuscript is
DOI:10.2151/jmsj.2025-017
J-STAGE Advance published date: February 19, 2025
The final manuscript after publication will replace the preliminary version at the above DOI once it is available.

Structure, trend and variability of the semiannual oscillation in the equatorial middle atmosphere in JRA-3Q and in satellite observations

Kiyotaka Shibata and Hiroaki Naoe

Meteorological Research Institute

February 4, 2025

Abstract

The Japanese Reanalysis for Three Quarters of a Century (JRA-3Q) with top at 0.01 hPa (high-top) is investigated focusing on the semiannual oscillation (SAO) in the tropical middle atmosphere, together with the other high-top reanalyses, ERA5 and MERRA-2, and the MLS and SABER satellite data. By removing the annual component and using the SAO component alone in the SABER data spanning the recent two decades, the seasonal cycle of the mesospheric SAO (MSAO) at 0.01 hPa is found to have significantly larger first cycle than the second cycle in a year with the largest easterly wind in boreal spring. The seasonal cycle of the stratospheric SAO (SSAO) at 1 hPa shows commonly in both satellite data that the easterly wind amplitude in boreal winter is double as large as that in boreal summer, while the westerly wind amplitudes in boreal spring and autumn are nearly the same. The two satellite data exhibit that the MSAO amplitude has significant and negative trend, about −5 and −7 m s^{-1} $decade^{-1}$ at 0.01 hPa in MLS and SABER, respectively. JRA-3Q reproduces well the seasonal cycle of the SAO, i.e., the calendar-locked downward propagation of the SAO from 0.01 hPa to 10 hPa with clear separation between the MSAO and SSAO, despite the MSAO being substantially underestimated compared to the satellite observations. The SSAO amplitude at 1 hPa is significantly increasing in JRA-3Q over about three decades from 1970s to 2000s, and it exhibits slight decreasing trend over the recent two decades from 2000s. Before 1970s the SSAO wavelet spectra are less concentrated around 6 months and the wavelet spectra around the annual component are significantly larger than those after 1970s in JRA-3Q and ERA5. None of the reanalyses show any hint of the MSAO significant and negative trend at 0.01 hPa.

Keywords: JRA-3Q; MLS; SABER; SAO; middle atmosphere; reanalysis

1. Introduction

The atmospheric reanalysis provides temporally and spatially uniform data by assimilating various observations such as surface, radio sonde, ship and satellite, which are irregularly distributed in space, with a single numerical forecast model of the same version throughout one specified long term. This single forecast model assimilation over a lengthy period gives temporal and spatial consistency to the reanalysis data, which hence is free from abrupt inhomogeneities and discontinuities stemming from changes in assimilation methods and in retrieval algorithms. However, there arise inevitably errors due to changes in the quality and/or quantity of the input observation data (e.g., Fujiwara et al. 2017; SPARC 2022). The reanalysis data, nonetheless, comes to be indispensable for credible and accurate analyses of past atmospheric and climatic phenomena consequently. There are several reanalysis centers, which have issued global atmospheric reanalysis datasets. For example, European Centre for Medium-Range Weather Forecasts (ECMWF), Japan Meteorological Agency (JMA), National Aeronautics and Space Administration (NASA), National Oceanic and Atmospheric Administration (NOAA) / National Centers for Environmental Prediction (NCEP) of the NOAA. These centers have continually released update versions of their reanalyses in certain time intervals.

Following the first long-term reanalysis JRA-25 (Onogi et al. 2007) and the second one JRA-55 (Kobayashi et al. 2015; Harada et al. 2016), the JMA released the third one, the Japanese Reanalysis for Three Quarters of a Century (JRA-3Q) in late 2023 (Kosaka et al. 2024). One major advantages of JRA-3Q over JRA-55 is the longer (by ~10 years) period starting from September 1947 and the increase in horizontal and vertical resolutions with an extension of the vertical domain, i.e., higher model lid, in the global forecast model. The horizontal resolution becomes finer from ~55 km (triangular truncation wavenumber with linear grid of 319; TL319) to ~40 km (TL479) and the top level comes to be higher from 0.1 hPa to the mesopause of 0.01 hPa with an increase in the number of vertical levels from 60 to 100 (Kosaka et al. 2024). To be specific in the SAO altitude range above 10 hPa, JRA-55 has 14 intrinsic levels to 0.1 hPa, while JRA-3Q has 19 intrinsic levels to 0.01 hPa (15 levels to 0.1 hPa and 4 levels above). As a result, equatorial and gravity waves as well as Rossby waves propagating upward from the troposphere are expected to be better represented in the finer-grid and deeper atmosphere and so are their momentum depositions in the middle atmosphere in JRA-3Q, likely leading to more realistic atmospheric circulation, particularly in the upper stratosphere and mesosphere, where observation inputs for the assimilation are much less than below. Certainly, JRA-3Q reproduced larger (more realistic) semiannual components in zonal wind at the stratopause than JRA-55 (e.g., Kawatani et al. 2020; SPARC 2022).

In the equatorial upper stratosphere and mesosphere, the zonal wind reverses direction with a season(calendar)-locked 6–month period, and this semiannual oscillation (SAO) is the one of the dominant variabilities there. Below the SAO altitudes in the tropical stratosphere there is the quasi-biennial oscillation (QBO), wherein the westerly and easterly winds alternate with broad intervals from about 20 to 40 months, centered at about 28 months. In the SAO and QBO the atmospheric waves excited predominantly by strong convective activity in the troposphere play a crucial role in the forcing, because they can freely propagate upward to the middle atmosphere due to the weak Coriolis force in the tropics (e.g., Andrews et al. 1987). The SAO was first observed by rocket-sondes and radars at stations near the equator (e.g., Reed 1966; Groves 1972; Hirota 1978) and these observations indicate that the SAO can be divided into the stratopause (or stratospheric) SAO (SSAO) (Reed, 1966) and the mesopause (or mesospheric) SAO (MSAO) (Groves 1972). The SSAO covers the altitude range from about 40 to 60 km with maximum amplitude at about 50 km (~1 hPa), while the MSAO dominates at altitudes from about 70 to 90 km with maximum amplitude at about 80 km (~0.01 hPa).

The SSAO momentum budget is maintained mainly by the momentum deposition due to the equatorial and gravity waves excited in the troposphere and propagating upward, and by the momentum flow due to the mean meridional flow across the equator, as demonstrated by observation analyses (e.g., Hitchman and Leovy 1986; Ray et al. 1998), mechanistic models (e.g., Dunkerton 1979; Holton and Wehrbein 1980), and general circulation models (e.g., Hamilton and Mahlman 1988; Jackson and Gray 1994). The importance of cross-equatorial meridional flow in the mechanism of the SSAO is different from that of the QBO, while wave forcing contributes to both. In perpetual season simulations, in which there is no semiannual meridional flow between the two hemispheres, the SSAO cannot be reproduced (Shibata 2022). The SSAO in the dynamical field (wind and temperature) also induces the SSAO in the chemistry field such as ozone distribution (e.g., Maeda 1984; Ray et al. 1994), and thereby reproducing the SSAO wind and temperature as accurate as possible in the reanalysis is linked to the further understanding of the atmospheric chemistry in the middle atmosphere.

The SAO in the reanalysis has been investigated mainly for the SSAO (e.g., Kawatani et al. 2020; SPARC 2022) because the forecast models for the reanalysis did not have sufficient levels in the mesosphere, wherein the MSAO dominates. However, in recent years, there appeared high-top forecast models with better vertical resolution in the mesosphere (~50–80 km) and they contributed to new generation reanalysis datasets such as the fifth generation ECMWF atmospheric reanalysis of the global climate (ERA5) (Hersbach et al. 2020) by ECMWF, the Modern-Era Retrospective Analysis for Research and Applications, Version 2 (MERRA-2) (Gelaro et al. 2017) by NASA Global Modeling and Assimilation Office (GMAO), and JRA-3Q by JMA. Of these high-top reanalyses, Ern et al. (2021) analyzed the MSAO as well as the SSAO in ERA5 and MERRA-2 up to ~75 km and compared with those in the SPARC climatology (SPARC 2002; Randel et al. 2004) and satellite data such as Aura Microwave Limb Sounder (MLS) and Sounding of the Atmosphere using Broadband Emission Radiometry (SABER) up to ~90 km. The ERA5 SAO is also reported up to 0.01 hPa (~80 km) in SPARC (2022) or equivalently, in the ECMWF website (https://confluence.ecmwf.int/display/CKB/ERA5%3A+The+QBO+and+SAO**).**

As stated before, the high-top (0.01 hPa) reanalysis data of JRA-3Q is just recently released in late 2023 and thus the performance of the JMA reanalysis data for the SAO is investigated only in the previous version JRA-55 (e.g., Kawatani et al. 2020; Ern et al. 2021; SPARC 2022). In line with the new release of JRA-3Q, this paper is to investigate both the SSAO and MSAO in JRA-3Q up to the mesopause (~0.01 hPa), together with those in the ERA5, MERRA-2, MLS, and SABER data, including the long-term trend and variability. The properties of the QBO in JRA-3Q is to be presented in another paper (Naoe et al. 2025). In this paper, the SAO is literally defined and extracted as the component which covers the spectrum, approximately centered at 6 months, from 3 to 8 months. By this preprocessing the seasonal cycle of the SAO comes to be free from the effect of the annual component. This is because the seasonal cycle made by the same month average of unfiltered data over multiyear inevitably includes not only the semiannual component but also the annual component significantly, depending on the altitudes, as demonstrated later. The rest of this paper is organized as follows. Section 2 describes the details of the reanalysis data and satellite data, and the methods in processing these data. Section 3 gives the results, wherein the climatological seasonal cycle, trend, and variability of the SAO in the recent two decades are presented. A discussion on the SSAO trend and behavior in JRA-3Q and ERA5 over longer time scales from 1950s or 1960s are provided in Section 4, and the conclusions are presented in Section 5.

2. Data and methods

2.1 Satellite observations and reanalysis data

In this study all the quantities are zonally averaged, so that we omit the term “zonal mean” in all the variables. The four seasons are referred to the boreal ones, i.e., spring means March–May, and so on. As observation data, we used upper-stratospheric and mesospheric temperatures retrieved primarily from bands near O_2 spectral lines at 118 GHz and 239 GHz measured by the MLS instrument on the Aura satellite, together with winds calculated from the MLS geopotential height data. Both the MLS temperature and geopotential height data were taken from level 3 monthly binned datasets of version 5.0x (Livesey et al. 2022), the latitudinal resolution of which is 4 degrees with the center latitude at the equator (they are available on line from https://acdisc.gesdisc.eosdis.nasa.gov/data/Aura_MLS_Level3/). The vertical resolution varies with altitude. For example, 13 pressure levels from 10 to 1 hPa; 6 pressure levels from 1 to 0.1 hPa; and 3 pressure levels from 0.1 to 0.01 hPa. The MLS data covers about two decades (~19.5 years) from August 2004 to December 2023 in the present study.

We also utilized the SABER data, i.e., the data measured by SABER on the TIMED (Thermosphere Ionosphere Mesosphere Energetics and Dynamics) spacecraft, version 2.0 level 2A pressure-level data for years from January 2002 to December 2023 (they are available on line from https://data.gats-inc.com/saber/custom/Temp_O3_H2O/v2.0/). The SABER data along satellite orbits are averaged every day in bins of 24° in longitude, 5° in latitude, and 2 km in log-pressure vertical coordinates. To remove local-time variation components including diurnal and semi-diurnal tides, we followed the method of Iwao and Hirooka (2021) and compiled monthly and zonal mean temperature and geopotential height data from 2002 to 2023.

The MLS and SABER zonal wind off the equatorial area is calculated from the geopotential height data using the gradient wind balance equation, which is a quadratic equation of zonal wind and represents that the pressure-gradient force balances the Coriolis force and the centrifugal force. Randel (1987) demonstrated that the gradient wind yielded good performance in the middle atmosphere. On the other hand, in the vicinity of the equator the gradient wind can introduce large errors because of the smallness in the meridional gradient of the geopotential height (Smith et al., 2017). So that, the zonal wind immediately near the equator is evaluated through cubic spline interpolation of the gradient wind outside the near-equator latitudes as in Smith et al. (2017). To be specific, the MLS equatorial zonal winds at 0 and ±4 degrees were interpolated from the gradient winds at ±8 and ±12 degrees. We used the MLS geopotential height data mostly up to 0.01hPa unless otherwise specified. This is because the MLS data (version 4.2) above 0.01hPa were not recommended for use due to too much noisiness in wind calculations at the equator (Smith et al. 2017). We followed this as for the version 5.0x MLS data. The SABER zonal wind is also obtained from geopotential height using the same method as that for the MLS data except that the equatorial zonal winds at 0 and ±5 degrees were interpolated from the gradient winds at ±10 and ±15 degrees.

In addition, the high-top (0.01hPa) reanalyses JRA-3Q, ERA5 and MERRA-2 are also analyzed, which span a period from 1948 to 2023 for JRA-3Q, from 1940 to 2023 for ERA5 and from 1980 to 2023 for MERRA-2. The latitudinal resolution of these three high-top reanalysis data is commonly 1.25 degrees, while the number of vertical layers in the SAO altitude range, from 10 to 0.01 hPa, is 11 for JRA-3Q and ERA5, and 14 for MERRA-2. Furthermore, previous versions of the JMA and ECMWF reanalyses, i.e., JRA-55, ERA-Interim (Dee et al. 2011), and ERA-40 (Uppala et al. 2005) are also used for comparison, although not shown.

2.2 Method of filtering, trend analysis, and lagged correlation

In the tropical upper stratosphere and mesosphere, the power spectrum analysis demonstrates that the SAO is the most dominant variability and the ANN is the second but modest variability (not shown). In addition, the phase of the ANN of zonal wind varies rather little with altitude and is approximately antisymmetric about the equator (Garcia et al, 1997), being in a distinct contrast to the phase of the SAO, which results in very small ANN amplitude when averaged over the tropical latitudes straddling the equator. Hence, the seasonal (or annual) cycle, i.e., multiyear average over the same month, of temporally unfiltered zonal wind has been interpreted to represent the SAO in most papers (e.g., Garcia et al. 1997; Smith et al. 2017; Kawatani et al. 2020; Ern et al. 2021; SPARC 2022), despite not explicitly referred to so. However, filtered zonal wind and temperature are also used in evaluating the SAO amplitudes (Kawatani et al. 2020; SPARC 2022), resulting in some ambiguity in the SAO evaluation. As demonstrated below, the effect of the ANN on the seasonal cycle of SAO is not necessarily small enough to be neglected except over the equator.

We defined the SAO as signals possessing periods from 3 to 8 months, and the annual component (ANN) as those from 9 to 15 months in this study. The SAO and ANN are derived by the Lanczos bandpass filter (Duchon 1979) with the cutoff periods mentioned above. On the other hand, to investigate the temporal behaviors of the SAO and ANN amplitudes, their amplitudes are obtained by the wavelet transform method, which provides a temporally local spectrum as used in the QBO analyses (e.g., Fischer and Tung 2008; Shibata and Deushi 2012).

In the wavelet transform method, a Morlet mother wavelet (plane wave modified by a Gaussian envelope) with non-dimensional frequency ω_0=6 (e.g., Torrence and Compo 1998) was used, so that the result of the wavelet analysis incorporates average information within approximately three cycles centered at the time and frequency concerned. After the wavelet calculation, wave amplitude in a narrow spectral interval was evaluated from the square root of its wavelet power, assuming a monochromatic wave as in Shibata and Naoe (2022). Namely, the SAO amplitude is evaluated as a square root of $2 \cdot P_{SAO}$, where P_{SAO} is the sum of the SAO wavelet power spectra between 3 and 8 months. The ANN amplitude is similarly calculated from the sum of ANN wavelet power spectra P_{ANN} between 9 and 15 months as a square root of $2 \cdot P_{ANN}$.

A regression line is calculated for the SAO amplitude to obtain its trend, in which the slope and intercept were evaluated by Sen’s slope estimator (Sen 1968) and the method by Siegel (1982), respectively. This is because Sen’s slope estimator is significantly more robust than the least squares method, because the former is insensitive to outliers. Statistical significance of the trends was made using the Mann–Kendall test for Sen's slope estimator.

Lagged correlation coefficients of the SAO amplitude between a reference altitude and other altitudes are calculated, and a statistical test of the correlation coefficients is evaluated by a Monte-Carlo simulation with phase randomization (e.g., Minobe and Nakanowatari 2002; Shibata and Naoe 2020). In the simulation, a large number (10,000 in this study) of surrogate time series are generated by an inverse Fourier transform with the same power spectra as the original time series at the reference altitude but with random phases, and then, surrogate correlation coefficients between the two time-series are calculated. The relative position of the real correlation coefficient in the sorted distribution of the surrogate correlation coefficients gives the level of confidence.

3. Result

3.1 Climatological SAO in the MLS and SABER data

Figure 1 depicts the latitude-height cross sections of the SAO amplitudes, obtained through the wavelet transform method, of the MLS and SABER zonal winds and temperatures from 10 to 0.005 hPa between 30°S and 30°N for the periods 2004–2023 and 2002–2023. The reason of expanding the figure top as high as to 0.005 hPa is to qualitatively confirm that the MSAO maximizes around or just below the mesopause altitude (~0.01 hPa) for zonal wind and temperature. The MSAO (the maximum at 0.015 hPa) and SSAO (the maximum at 1 hPa) of the

MLS zonal wind are both asymmetric with respect to the equator, and the SSAO shows larger asymmetry and wider latitudinal extent than the MSAO. On the other hand, in the SABER zonal wind the MSAO is symmetric and the SSAO exhibits weakly asymmetric structure with both being of similar latitudinal extent. The peak values of the MSAO are about 25 m s^{-1} around 0.015 hPa and 5°S for MLS and about 30 m s^{-1} around 0.01 hPa over the equator for SABER, while the peak values of the SSAO are commonly about 30 m s^{-1} around 1 hPa but at different latitudes, 12°S for MLS and 8°S for SABER.

The MSAO and SSAO amplitude of temperature are almost symmetric with respect to the equator maximizing over the equator both in MLS and SABER, while the MSAO amplitude is much stronger and wider than the SSAO amplitude. The peak values of the MSAO amplitude at about 0.02 hPa is about 7 K for MLS and about 8 K for SABER, while those of SSAO is commonly about 4.5 K at about 2 hPa. The MSAO and SSAO altitudes of temperature peaks are slightly lower than those of the zonal wind peaks. The SSAO amplitudes of zonal wind and temperature are quantitatively very similar to those evaluated from the standard deviation of the SSAO (of filtered zonal wind or temperature) time series (Kawatani et al. 2020; SPARC 2022).

Figure 2 displays the latitude-height cross sections of the ANN amplitudes of the MLS and SABER zonal winds and temperatures from 10 to 0.01 hPa between 30°S and 30°N. The ANN amplitude of zonal wind minimizes to about 10 m s^{-1} over the equator with slight vertical variations. In the tropics within ~20 degrees of the equator the ANN amplitude is larger in NH than in SH in the upper mesosphere from 0.2 to 0.02 hPa, while the ANN amplitude is small in NH than in SH from the upper stratosphere (~5 hPa) to the lower mesosphere (~0.5 hPa). The ANN amplitude of temperature shows very weak latitudinal variations within ~15 degrees of the equator above the middle mesosphere of 0.2 hPa with peak value of about 3 K around 0.05 hPa. Below 0.2 hPa also the latitudinal variations of the ANN amplitude are weak in the vicinity of the equator.

Figure 3 exhibits the month-latitude cross sections of the climatological MLS and SABER unfiltered zonal winds at 0.01 hPa and 1 hPa between 30°S and 30°N, wherein the climatological annual mean is subtracted at each latitude. These plots in Fig. 3 represent the seasonal cycle of the MLS and SABER zonal winds at respective altitude, and the plots at the stratopause altitude of 1 hPa (Figs. 3b and 3d) are very similar to the analyses using slightly shorter MLS and SABER data (Smith et al. 2017; Kawatani et al. 2020). It is evident that the zonal wind near the equator reverses direction four times a year, demonstrating the dominance of the SAO. In addition, the zonal wind directions between 1 and 0.01 hPa are almost opposite phase, corresponding to the phase relation between the SSAO and MSAO.

However, the seasonal cycles in Fig. 3 created through averaging the same month data, i.e., average at 12-month interval, inevitably include both 6-month and 12-month components. Namely, the plots in Fig. 3 draw the seasonal cycles not due to the SAO alone but due to both the SAO and ANN. The ANN and SAO seasonal cycles of the MLS and SABER zonal winds at 0.01 and 1 hPa are displayed in Figs. 4 and 5, respectively. The ANN wind shows approximately so simple antisymmetric pattern between the summer and winter hemispheres that there blow easterlies in the summer hemisphere and westerlies in the winter hemisphere with near-zero wind latitude areas at the boundaries, which are situated spatially close to the equator and temporally close to the equinoxes (Fig. 4). The near-zero wind area corresponds to the minimum wind amplitude area in the vicinity of the equator (Figs. 2a and 2c). It should be noted that the latitudinal profile of the ANN zonal wind slightly deviates from antisymmetricity, depending on altitudes. Hence, this deviation results in small but significant contribution to the seasonal cycle of the zonal wind latitudinally averaged across the equator, which systematically varies with altitudes as shown later.

In the SAO seasonal cycle, the MLS and SABER zonal wind (Fig. 5) varies more slightly with latitudes than the unfiltered zonal wind near the equator, in particular at 0.01 hPa (Fig. 3), leading to more vertically aligned contours in Fig. 5 than in Fig. 3. In the MSAO wind at 0.01 hPa there are distinct differences between MLS and SABER. In the MLS data westerly phases during winter and summer are temporally rather symmetric to each other near the equator, about 5°S–5°N, and so do the easterly phases during spring and autumn, while the westerly winds are weaker with longer duration than the easterly winds. In contrast, in the SABER data the first cycle exhibit substantially larger amplitude than the second cycle, and the durations of easterly and westerly winds are similar. On the other hand, both satellite data are similar in SSAO at 1 hPa: the duration is nearly the same between the two phases. However, the SSAO easterly wind is much stronger in winter than in summer, while the westerly winds in spring and autumn show similar amplitudes, which are approximately an arithmetic mean of the two easterly amplitudes in winter and summer.

Figure 6 depicts the three seasonal cycles of the MLS and SABER zonal winds averaged between 10°S and 10°N from 10 to 0.01 hPa: unfiltered one without the annual mean, the ANN, and the SAO. In the stratosphere and lower mesosphere, i.e., the SSAO region, the seasonal cycle of the unfiltered zonal wind is evidently stronger in the first half of a year than that in the second half, precisely, westerly around January and easterly around April is stronger, in coincident with the SSAO characteristics described so far (e.g., Garcia et al. 1997; Kawatani et al. 2020). However, this is not necessarily the intrinsic SSAO characteristics, because the seasonal cycle of the ANN is approximately in phase in the first cycle (winter and spring at 1 hPa) but out of phase in the second cycle (summer and autumn at 1 hPa) with that of the SSAO below about 0.03 hPa (Fig. 6). Thus, the seasonal cycle of the SAO is accordingly strengthened in the first half and weakened in the second half, when those of the ANN and SSAO are combined together, as shown in Figs. 6a and 6d. Accordingly, the SSAO intrinsically possesses almost symmetric westerly phases and asymmetric easterly phases. In other words, when the ANN is removed, i.e., the SSAO has nearly symmetric westerly phases in spring and autumn, while the SSAO shows significant asymmetry in the easterly phases, wherein the peak value at 1 hPa is about 50% larger in winter than in summer, as evidently plotted in Fig. 7.

Near the tropics the MSAO above the middle mesosphere is out of phase to the SSAO (Figs. 6c and 6f) with peaks below the mesopause broadly extending from 0.02 to 0.01 hPa (Figs. 1a and

1c). There is substantial difference in the MSAO seasonal cycle between MLS and SABER. The MLS MSAO at 0.01 hPa is temporally symmetric in a year, i.e., the first cycle and the second cycle are very similar to each other, while the first cycle is significantly larger than the second cycle in the SABER MSAO (Fig. 7). In particular, the easterly wind in spring shows the largest amplitude, and this reflects the occasional occurrences of the mesospheric spring equinox enhancements (MSEE) analyzed in the radar observation data (Kishore Kumar et al. 2014), in which MSEE occurred in six years out of 20 years from 1993 to 2012. Further, there is another clear asymmetry between the two cycles of the MSAO at about 0.02 hPa commonly in both satellite data. The easterly and westerly winds in the second cycle maximize at lower altitude of 0.02 hPa than those in the first cycle, which maximize at 0.01 hPa (Fig. 6). So that, it is more preferable to depicts the SAO seasonal cycle over the whole months in a year rather than over one cycle (6 months) (Kumar et al. 2011) not only for the SSAO but also for the MASO.

3.2 Climatological SAO in the JRA-3Q, ERA5, and MERRA-2 data

Figure 8 exhibits the latitude-height cross sections of the SAO amplitudes of zonal wind and temperature for JRA-3Q, ERA5, and MERRA-2 from 10 to 0.01 hPa between 30°S and 30°N, in which the analysis period is 2004–2023 for JRA-3Q and ERA5, and 2005–2023 for MERRA-2. This one-year shorter period for MERRA-2 is to avoid conspicuous discontinuity above 2 hPa between 2004 and 2005, which can be seen in the monthly and globally averaged temperature anomaly (Gelaro et al. 2017), and also in the monthly averaged temperature in the tropics (not shown).

The MSAO amplitude of the JRA-3Q zonal wind maximizes at the mesopause altitude (0.01 hPa) as in MLS and SABER, though its peak value (~22 m s^{-1}) is moderately weaker and latitudinal width is much narrower. The SSAO amplitude around the stratopause altitude is approximately close to those of MLS and SABER with respect to intensity (~28 m s^{-1}) and latitudinal extent. The MSAO amplitude of the JRA-3Q temperature maximizes not at 0.01 hPa but at 0.1 hPa in the tropics with smaller value (~5 K) than those of MLS and SABER. On the other hand, the SSAO amplitude the JRA-3Q temperature is very similar to those of MLS and SABER with respect to intensity and latitudinal and vertical extent.

The MSAO amplitude of the ERA5 zonal wind is very different from those of MLS and SABER. It has a peculiar bulge (~35 m s^{-1}) around 0.1 hPa over the equator with its axis extending downward and merging with the SSAO region. The SSAO amplitude of the ERA5 zonal wind is approximately similar to those of MLS and SABER with slightly stronger peak value. The MSAO amplitude of the ERA5 temperature shows much smaller peak value (~4 K) at about 0.05 hPa than those of MLS and SABER, while the SSAO amplitude is very close to those of MLS and SABER. In the MERRA-2 zonal wind the SAO amplitude monotonically decreases with altitude above 0.5 hPa in the tropics, indicating no distinct but blurred MSAO in zonal wind. In contrast, the SAO amplitude of the MERRA-2 temperature maximizes to ~4 K at about 0.02 hPa, demonstrating a clear MSAO in temperature. The SSAO meridional structure of the MERRA-2 zonal wind is slightly different from the satellite observations, while that of the MERRA-2 temperature is similar. The SSAO amplitude within 10 degrees of the equator is realistically reproduced in zonal wind and temperature as those in JRA-3Q and ERA5.

The three reanalyses, JRA-3Q, ERA5, and MERRA-2, simulate well the observed relation of the SSAO structures between zonal wind and temperature, i.e., zonal wind peak at 1 hPa and temperature peak at 2 hPa. On the other hand, none of the reanalyses can reproduce the observed relation of the MSAO structures, particularly much deteriorated in the zonal wind. This is probably due to some artificial forcing and/or damping in the near-top layers for stable time integration of the forecast model, resulting in a balance between zonal wind and temperature being different from the observed structure.

Figure 9 depicts the SAO zonal winds at 0.01hPa, and 1 hPa of JRA-3Q, ERA5, and MERRA-2, respectively. The seasonal cycle of the SSAO wind at 1 hPa in the MLS and SABER data (Figs. 5b and 5d) is approximately reproduced in the three reanalyses at each latitude. On the other hand, the three reanalyses have different performance for the seasonal cycle of the MSAO wind at 0.01 hPa in the MLS and SABER data (Figs. 5a and 5c). In JRA-3Q the phase of the MSAO wind at 0.01 hPa (Fig. 9a) is correctly reproduced to be opposite to that of the SSAO wind at 1 hPa (Fig. 9b) and the MSEE-related intensification is also simulated despite the easterly wind being about half of the observed value in the SABER wind (Fig. 5c). In ERA5 the seasonal cycle of the MASO wind at 0.01 hPa (Fig. 9c) is shifted not observed ~π but ~$\pi/2$ from that of the SSAO wind at 1 hPa (Fig. 9d). In MERRA-2 the seasonal cycle of the MASO wind (Fig. 9e) is nearly in phase with that of the SSAO wind (Fig. 9f). Of the three reanalyses, ERA5 and MERRA-2 severely underestimated the features of the MSAO amplitude.

In the vertical cross section of the seasonal cycle of the SAO wind in the three reanalyses (Fig. 10) the phase descent with time from 0.01 to 10 hPa is realistically reproduced in JRA-3Q with separation between the MSAO and SSAO regions around 0.1 hPa, despite insufficient difference in the strength of the MSAO easterly wind between the first and second cycles as stated above. In ERA5 the SAO phase descent with time from 0.01 hPa does not persist down to 10 hPa but ceases at about 0.05 hPa, below which the phase temporal procession is reverted, i.e., the phase ascends with time from 1 to about 0.05 hPa (Fig. 9b). This phase ascent with time in the mesosphere of ERA5 can also be seen in the seasonal cycle of the unfiltered zonal wind (Ern et al. 2021; SPARC 2022), which is comprised dominantly of the SAO, ANN and the annual mean. MERRA-2 simulates generally well the SSAO seasonal cycle (Fig. 10c). Still, zonal wind weakens to below 10 $\mathrm{m\ s^{-1}}$ abruptly above ~0.3 hPa up to 0.05 hPa. The MSAO amplitude of the MERRA-2 zonal wind is much weaker over deep layer above ~0.3 hPa than the observations. The MSAO seasonal evolution is opposite to the observations from about 0.05 to 0.01 hPa, i.e., the phase propagates upward with time, though below about 0.05 hPa there are downward phase propagations continuing to the SSAO phases as in the observations (Fig. 10c).

3.3 SAO amplitude trend and intraseasonal variability

In this section we investigate the SAO linear trend together with its intraseasonal variations for the MLS period 2004–2023 and for the SABER period 2002–2023, notwithstanding that the period length of about 20 years is not necessarily long enough for the trend evaluation. In the trend calculation, the SABER zonal wind and temperature are interpolated to the same altitudes as those of the MLS data. Figure 11 depicts the vertical cross section (10–0.01 hPa) of the time evolution of the SAO amplitudes of MLS and SABER zonal winds and temperatures averaged between 10°S and 10°N. In the amplitude variations there are approximately two periods independently in the MSAO and SSAO, that is, short period of 1–2 years and long period of 3–4 years. The short period variations have relatively small vertical extent so that they remain within the MSAO or SSAO altitudes, respectively. On the other hand, the long period variations tend to be tall, and thereby sometimes they are connected between the MSAO and SSAO altitudes, such as around 2006, 2010, 2013, 2016, 2019.

Figure 11 also shows that the MSAO temperature amplitude immediately below the mesopause is significantly decreasing, while the SSAO temperature amplitude just below the stratopause scarcely exhibits significant long-term change. The long-term trends in the MSAO and SSAO zonal wind are quantified through evaluating linear fitting at each altitude. Figure 12 displays the vertical profiles of the linear trends in the SAO amplitudes of the MLS and SABER zonal wind and temperature along with the statistical significance. It is evident that the MSAO wind amplitude is declining with a peak of about −5 and −7 m s^{-1} decade^{-1} in the MLS and SABER data around 0.01 hPa accompanied by significant negative trend in the temperature amplitude of about −1 K decade^{-1} in 0.02–0.04 hPa. Both MSAO negative trends in zonal wind and temperature are statistically significant exceeding the 99% level, indicating that the MSAO is significantly weakening over the recent two decades.

The SSAO amplitude of zonal wind also shows significant negative trend of about −1 and −2 m s^{-1} decade^{-1} in the MLS and SABER data around 0.8 hPa accompanied by negative trend in the temperature amplitude of about −0.3 K decade^{-1} around 1 hPa. On the other hand, the SSAO amplitudes of the two satellite data have similar positive trend of about 0.1 K^{-1} decade^{-1} around 10 hPa. However, the corresponding trends in the SSAO amplitude of zonal wind do not agree to each other. Similarly, the two SSAO zonal wind amplitude trends substantially differ around 2 hPa, where SABER shows about +1 m s^{-1} decade^{-1} with 99% significance but MLS indicates almost no trend.

Figure 13 exhibits the vertical profiles of the linear trends in the SAO amplitudes of JRA-3Q, ERA5, and MERRA-2. Just below the mesopause region ERA5 reproduced the significant negative trends at 0.03 hPa for both temperature and zonal wind, and MERRA-2 reproduced them at 0.01 and 0.03 hPa. However, their trends of the zonal wind were too small and the relations between the zonal wind and temperature trends did not resemble the observations Hence, none of the reanalyses reproduced the significant negative trends of the MSAO around 0.01 hPa for zonal wind and around 0.02–0.04 hPa for temperature. The observed negative trends of the SSAO amplitudes around 0.8 hPa for zonal wind around 1 hPa for temperature are simulated both in JRA-3Q and MERRA-2, while ERA5 simulates the negative trend of temperature alone with almost zero or positive trend in zonal wind around 0.8 to 1 hPa.

3.4 Lagged correlation of the SAO amplitude

Since the SAO momentum budget is maintained mainly through the momentum deposition due to upward propagating waves, i.e., wave-mean flow interaction (e.g., Holton and Wehrbein 1980; Hitchman and Leovy 1986; Jackson and Gray 1994), the SAO variations at one level could affect those at other levels. So, to investigate the extent of the SAO variability in time-altitude domain, we evaluate the lagged correlation of the SAO amplitude between different altitudes, in which the reference altitude is taken at the maximum amplitude altitude of the SSAO, i.e., at 1 hPa for zonal wind and at 2 hPa for temperature. Figure 14 represents the lagged correlation coefficients for the detrended SAO amplitudes of the MLS and SABER zonal wind and temperature in the lag-altitude space, wherein the lag is from −12 to +12 months and positive (negative) lags mean retarded (advanced) phases from the phase at the reference altitude. Since the lag imposed is within 12 months, Fig. 14 shows the lagged correlation of the intraseasonal variations in the SAO amplitude. The statistical significance is calculated at each lag by the Monte-Carlo simulation with phase randomization (e.g., Minobe and Nakanowatari 2002; Shibata and Naoe 2020) as stated before.

In the SABER zonal wind, gradual downward propagation of the significant correlation can be clearly seen from -4 months at 0.2 hPa to +5 months at 3 hPa (Fig. 14c), indicating the SSAO intraseasonal variations remain within the SSAO altitude range. However, the downward propagation time is much longer than that of the SAO itself, which is about 2 months from 0.2 to 3 hPa (Fig. 6f). In addition, Fig. 14c demonstrates that the MSAO intraseasonal variations at 0.02 hPa advance the SSAO intraseasonal variations at 1 hPa with lead time of 12–10 months in the SABER data. Also in the MLS data, the MSAO intraseasonal variations at 0.02 hPa shows significant correlation with the SSAO ones, but the high correlation area diminishes around 0.1 hPa.

In the temperature data, significant correlation area is vertically narrower than that in zonal wind data, but within about ±3 months lag significant correlation area extends upward to about 0.2 and 0.05 hPa for MLS and SABER, resulting in high correlation vertical range being approximately similar to that of zonal wind. However, a close inspection indicates that there are some notable differences in the lag for zonal wind and the lag for temperature, albeit the SAO zonal wind and temperature structures being dynamically consistent. These differences may stem from errors in observation (retrieval), and those in zonal wind calculation algorithm.

Figure 15 exhibits the lagged correlation coefficients for the detrended SAO amplitudes of zonal wind and temperature in JRA-3Q, ERA5, and MERRA-2 as in Fig. 14. JRA-3Q reproduces a thick pattern of large correlation coefficients of greater than 0.4 within ±4 months lag below about 0.2 hPa for the zonal wind amplitude, while above 0.1 hPa the axis of large correlation is leaning toward positive lags with altitudes, opposite to that in the observed data. In temperature amplitude in JRA-3Q the large correlation coefficients (> 0.4) area is confined below 0.5 hPa, i.e., too shallow, compared to those in the observed data. In ERA5 the large correlation coefficients (> 0.4) area in the zonal wind amplitude shows a less vertical extension to the mesosphere but extends in temporal direction more to about ±6 months lag, indicating that the intraseasonal variation in the zonal wind amplitude near the stratopause is temporally wider and scarcely correlated with that in the mesosphere. The intraseasonal variation in the ERA5 temperature amplitude also exhibits shallower and wider pattern of large correlation, being consistent characteristics with that in the wind amplitude. In MERRA-2 the large correlation coefficients (> 0.4) area extends deep into the mesosphere up to about 0.1 hPa within ±(4–5) months lag for both zonal wind and temperature, reproducing good intraseasonal variations in SSAO.

Figures 14 and 15 also show the autocorrelations of the SSAO amplitudes at the reference altitudes, 1 hPa for zonal wind and 2 hPa for temperature. The lagged correlations at these altitudes, i.e., the autocorrelations, are positive and significant within approximately ±(4–6) months lag for the satellite observations and the reanalyses. This indicates that the successive SSAO amplitudes at these altitudes are not fully independent to each other but positively correlated. In other words, if a SSAO amplitude is larger (smaller), then the following one tends to be also larger (smaller).

4. Discussion

JRA-3Q can relatively well reproduce the calendar-locked downward propagation of the SAO from the mesopause to the upper stratosphere of ~10 hPa with separation at about 0.1 hPa between the MSAO and SSAO (Fig. 10a). However, quantitative examination reveals that the MSAO in JRA-3Q is very different, particularly above the middle mesosphere, from the satellite observations with respect to the vertical profiles of the MSAO zonal wind and temperature amplitudes, as can be readily seen from a comparison between Figs. 1a–d and Figs. 8a, 8b. In addition, the evident and significant negative trends in the MSAO in the upper mesosphere (Figs. 12a–d) cannot be captured at all in JRA-3Q (Figs. 13a and 13b). The other reanalyses possess much severer drawbacks in the seasonal cycle of the SSAO above the stratopause and MSAO: superfluous upward propagation of the phase between 1 to about 0.05 hPa in ERA5 (Fig. 10b), and between 0.05 and 0.01 hPa in MERRA-2 (Fig. 10c).

On the other hand, below the stratopause the seasonal cycle of the SSAO is fairly realistically simulated not only in JRA-3Q, ERA5, and MERRA-2 but also in JRA-55 and ERA-Interim. Indeed, artificial treatments in the numerical calculation near the upper boundary of the forecast model for the stable time integration are partly responsible for the above-mentioned low and/or erroneous performance for the SAO in the mesosphere, but the scantiness of observation data assimilated in the mesosphere is also likely involved. So that, incorporating the limb sounding data such as the MLS and SABER data in the assimilation is preferable as in Koshin et al. (2020, 2022) to simulate the SAO in the mesosphere as realistically as possible, although the assimilation of the limb sounding data does not necessarily lead to better representation of SAO as in MERRA-2, which assimilates the MLS data (Gelaro et al. 2017). The fact that MERRA-2 does not reproduce the realistic MSAO indicates the effect of some artificial treatment near the forecast model top is much larger than that of assimilation.

So far, we investigated the SAO properties over the recent two decades of the MLS and SABER data. Next, we extend the period to the whole terms of the three reanalyses, i.e., 1948–2023 for JRA-3Q, 1940–2023 for ERA5, and 1980–2023 for MERRA-2, and focus on the SSAO only below the stratopause. This is because the SAO in the reanalysis above the stratopause is expected to be all the more biased in the past period before 2000 than in the recent two decades, when the SAO in the mesosphere is barely or scarcely reproduced (Figs. 10a–c). This is because the satellite observations assimilated in the reanalysis before about 1995 are much smaller than those after 1995 (e.g., Hersbach et al. 2020; Kosaka et al. 2024).

Figure 16 depicts the time series of the amplitude spectra of the JRA-3Q zonal wind at 1 hPa, and temperature at 2 hPa from 3 to 15 months period, along with those of ERA5 and MERRA-2. The SSAO amplitudes of the JRA-3Q zonal wind and temperature, which correspond to the spectra approximately centered at 6 months from 3 to 8 months in Figs. 16a and 16b, show slight decreasing trends in the recent two decades between around 2005 to 2023, while the SSAO amplitudes are steadily increasing with small ups and downs from around 1975 to 2005. On the other hand, before around 1975 the SSAO amplitudes show negative trends and the amplitude spectra are not concentrated in the vicinity of 6 months but spread to shorter and longer periods. That is, the SSAO spectral shape after around 1975 shows significantly steeper and larger peak than that before. In addition, the ANN amplitude becomes conspicuously large, relatively to the SSAO amplitude, in temperature at 2 hPa before 1975.

In ERA5 the SSAO amplitudes of zonal wind at 1 hPa and temperature at 2 hPa exhibit slight positive and negative trends, respectively, in the recent two decades, and prior to this period from around 1965 to 2005 the SSAO amplitudes show positive trends (Figs. 16c and 16d). Before around 1965, the SSAO amplitudes show negative trends. The SSAO spectral shape after around 1965 shows significantly sharper and larger peak than that before. The ANN amplitude of temperature is evidently larger before 1995 than after. These positive trends of the JRA-3Q and ERA5 SSAO amplitudes of zonal wind at 1 hPa and temperature at 2 hPa during the three or four decades before about 2005 can be similarly seen in the previous reanalyses, JRA-55 and a combined data of ERA-Interim and ERA-40 (not shown). The SSAO amplitudes of the MERRA-2 zonal wind at 1 hPa and temperature at 2 hPa show slight negative trends in the recent two decades. There are similar negative trends from 1980 to around 2002, but the SSAO amplitudes discontinuously increased about 5 m s^{-1} and 1 K for zonal wind and temperature around 2002.

Indeed, these long-term trends of the SSAO amplitudes at and just below the stratopause are consistent between zonal wind at 1 hPa and temperature at 2 hPa in JRA-3Q and ERA5, respectively, but their reliability is disputable, in particular, before 1979 when no satellite observation was available. During 1960s and 1970s the SSAO is very weak in the two reanalyses, which reflects accurately the intrinsic limited capability to simulate the SSAO in the forecast models used for the assimilation. Similarly, the SSAO is not necessarily well reproduced in the simulations with state-of-the-art general circulation models reproducing the QBO (Smith et al. 2020), indicating the need for further improvement above the upper stratosphere in global models.

The other causes may also be involved because the SSAO amplitude at 1hPa shows a gradual increase backward before 1975 in JRA-3Q and 1965 in ERA5 despite the SSAO amplitude itself is much smaller than that in recent two decades, as stated before. The rapid diminishing of the QBO backward before around 1970 in JRA-3Q (Naoe et al. 2025) and around 1960 in ERA5 is one possible cause of the gradual increase in the SSAO amplitude backward before 1975, because the QBO in the stratosphere modulates the SAO above the upper stratosphere and mesosphere (e.g., de Witt et al. 2013; Kishore Kumar et al. 2014; Smith et al. 2017). However, its mechanism is not yet comprehensively clarified. Anyway, the weaker wavelet spectrum peak of the SSAO before about 1975 for JRA-3Q (Figs. 16a and 16b) and about 1965 for ERA5 (Figs. 16c and 16d) strongly suggests that these gradual increases also stem from the forecast models themselves.

5. Conclusions

The Japanese third reanalysis version JRA-3Q with a high-top lid at 0.01 hPa is examined with respect to the SAO in the tropical middle atmosphere from 10 to 0.01 hPa, along with the ERA5 and MERRA-2 reanalyses and the MLS and SABER satellite data. Since the seasonal cycle of the raw (unfiltered) data created through averaging the same month at 12-month interval includes unavoidably the annual component as well as the semiannual component, applying a bandpass filter with cut-off periods at 3 and 8 months is performed to extract the SAO component.

The MLS data shows that the seasonal cycle of the MSAO at 0.01 hPa is very similar between the first cycle from winter to spring and the second cycle from summer to autumn, while the SABER data exhibits that the first cycle is significantly larger than the second cycle. In particular, the easterly wind in spring is the largest amplitude, corresponding to the occasional occurrence of MSEE. The seasonal cycle of the SSAO at 1 hPa in both satellite data proves that the easterly wind amplitude in winter is double as large as that in summer, while the westerly wind amplitudes in spring and autumn are nearly the same.

JRA-3Q is found to reproduce well the observed characteristics of the seasonal cycle of the SAO, i.e., the calendar-locked downward propagation of the SAO from 0.01 hPa to 10 hPa with clear separation between the MSAO and SSAO, despite the MSAO being underestimated. In the SAO of the ERA5 zonal wind the amplitude at 0.01 hPa is much underestimated and the phase descent from 0.01 hPa does not persist down to 10 hPa but ceases at about 0.05 hPa, below which the phase temporal procession is reverted, i.e., the SAO phase ascends with time from 1 hPa. The

MSAO amplitude of the MERRA-2 zonal wind is also much weaker than the observations and its seasonal evolution is opposite to the observations, i.e., the phase propagates upward with time from about 0.05 to 0.01 hPa.

The MSAO amplitude of zonal wind has significant negative trend of about −5 and −7 m s^{-1} $decade^{-1}$ in the MLS and SABER data, respectively, around 0.01 hPa accompanied by significant negative trend in the temperature amplitude of about −1 K $decade^{-1}$ in 0.02–0.04 hPa. This demonstrates that the MSAO is significantly weakening over the recent two decades. The SSAO amplitude of zonal wind also shows significant negative trend of about −1 and −2 m s^{-1} $decade^{-1}$ in the MLS and SABER data, respectively, around 0.8 hPa accompanied by negative trend in the temperature amplitude of about −0.3 K $decade^{-1}$ around 1 hPa. In addition, the SSAO amplitudes of the two satellite data have similar positive trend of about 0.1 K^{-1} $decade^{-1}$ around 10 hPa. However, the corresponding trends in the satellite SSAO amplitude of zonal wind do not agree to each other.

The SSAO amplitudes of zonal wind at 1 hPa and temperature at 2 hPa are substantially increasing in JRA-3Q and ERA5 from 1970s over about three decades, while they exhibit notable negative trends over the recent two decades except for the ERA zonal wind. Before 1970s the SSAO wavelet spectra is less concentrated around 6 months and the annual components are considerably larger than those after 1970s in JRA-3Q and ERA5.

Data Availability Statement

The JRA-3Q and JRA-55 reanalysis data are provided via collaborative organizations listed in the JRA website (https://jra.kishou.go.jp/). The ERA5, ERA-Interim, and ERA-40 reanalysis data can be obtained from the ECMWF website (https://www.ecmwf.int/en/forecasts/datasets/browse-reanalysis-datasets/). The ERA5 SAO figures are available from the ECMWF website (https://confluence.ecmwf.int/display/CKB/ERA5%3A+The+QBO+and+SAO**)**. The MERRA-2 reanalysis data can be obtained from the NASA website (https://disc.gsfc.nasa.gov/datasets/). The MLS level 3 data of temperature and geopotential height are available from the NASA website (https://acdisc.gesdisc.eosdis.nasa.gov/data/Aura_MLS_Level3/). The SABER level 2 data temperature and geopotential height are available on line from the aerospace company GATS (Global Atmospheric Technologies & Sciences) web site (https://data.gats-inc.com/saber/custom/Temp_O3_H2O/v2.0/).

Acknowledgments

The authors are grateful to Dr. Chiaki Kobayashi at the Meteorological Research Institute and Dr. Shingo Watanabe at the Japan Agency for Marine-Earth Science and Technology for their help in analyzing the ERA5 data. The authors are also particularly grateful to Professor Koki Iwao at National Institute of Technology, Kumamoto College for providing analysis programs for the SABER data. This study was partly supported by the Japan Society for the Promotion of Science KAKENHI (grant numbers: JP22H04493, JP24K07140, JP24K00710).

References

Andrews, D. G., J. R. Holton, and C. B. Leovy, 1987: *Middle Atmosphere Dynamics*. Academic Press, Orland, CA, USA, 489pp.

Dee, D. P., S. M. Uppala, A. J. Simmons, P. Berrisford, P. Poli, S. Kobayashi, U. Andrae, M. A. Balmaseda, G. Balsamo, P. Bauer, P. Bechtold, A. C. M. Beljaars, L. van de Berg, J. Bidlot, N. Bormann, C. Delsol, R. Dragani, M. Fuentes, A. J. Geer, L. Haimberger, S. B. Healy, H. Hersbach, E. V. Hólm, L. Isaksen, P. Kållberg, M. Köhler, M. Matricardi, A. P. McNally, B. M. Monge-Sanz, J.-J. Morcrette, B.-K. Park, C. Peubey, P. de Rosnay, C. Tavolato, J.-N. Thépaut, and F. Vitart, 2011: The ERA-Interim reanalysis: Configuration and performance of the data assimilation system. *Quart. J. Roy. Meteor. Soc.*, **137**, 553–597.

de Wit, R. J., R. E. Hibbins, P. J. Espy, and N. J. Mitchell, 2013: Interannual variability of mesopause zonal winds over Ascension Island: Coupling to the stratospheric QBO. *J. Geophys. Res. Atmos.*, **118**, 12 052–12 060, doi:10.1002/2013JD020203.

Dunkerton, T. J., 1979: On the role of the Kelvin waves in the westerly phase of the semiannual zonal wind oscillation. *J. Atmos. Sci.*, **36**, 32–41.

Duchon, C. E., 1979: Lanczos filtering in one and two dimensions. *J. Appl. Meteor.*, **18**, 1016–1022.

Ern, M., M. Diallo, P. Preusse, M. G. Mlynczak, M. J. Schwartz, Q. Wu, and M. Riese, 2021: The semiannual oscillation (SAO) in the tropical middle atmosphere and its gravity wave driving in reanalyses and satellite observations. *Atmos. Chem. Phys.*, **21**, 13763–13795, doi: 10.5194/acp-21-13763-2021.

ECMWF website, May 5, 2023: ERA5: The QBO and SAO, https://confluence.ecmwf.int/display/CKB/ERA5%3A+The+QBO+and+SAO.

Fischer, P. and K. K. Tung, 2008: A reexamination of the QBO period modulation by the solar cycle. *J. Geophys. Res.*, **113**, D07114, doi:10.1029/2007JD008983.

Fujiwara, M., J. S. Wright, G. L. Manney, L. J. Gray, J. Anstey, T. Birner, S. Davis, E. P. Gerber, V. L. Harvey, M. I. Hegglin, C. R. Homeyer, J. A. Knox, K. Krüger, A. Lambert, C. S. Long, P. Martineau, A. Molod, B. M. Monge-Sanz, M. L. Santee, S. Tegtmeier, S. Chabrillat, D. G. H. Tan, D. R. Jackson, S. Polavarapu, G. P. Compo, R. Dragani, W. Ebisuzaki, Y. Harada, C. Kobayashi, W. McCarty, K. Onogi, S. Pawson, A. Simmons, K. Wargan, J. S. Whitaker, and C. Zou, 2017: Introduction to the SPARC Reanalysis Intercomparison Project (S-RIP) and overview of the reanalysis systems. *Atmos. Chem. Phys.,* **17**, 1417–1452.

Garcia, R. R., T. J. Dunkerton, R. S. Lieberman, and R. A. Vincent, 1997: Climatology of the semiannual oscillation of the tropical middle atmosphere. *J. Geophys. Res.*, **102**, 26019–26032, doi:10.1029/97JD00207.

Gelaro, R., W. McCarty, M. J. Suárez, R. Todling, A. Molod, L. Takacs, C. A. Randles, A. Darmenov, M. G. Bosilovich, R. Reichle, K. Wargan, L. Coy, R. Cullather, C. Draper, S. Akella, V. Buchard, A. Conaty, A. M. da Silva, W. Gu, G.-K. Kim, R. Koster, R. Lucchesi, D. Merkova, J. E. Nielsen, G. Partyka, S. Pawson, W. Putman, M. Rienecker, S. D. Schubert, M. Sienkiewicz, and B. Zhao, 2017: The modern-era retrospective analysis for research and applications, version 2 (MERRA-2). *J. Climate*, **30**, 5419–5454, doi:10.1175/JCLI-D-16-0758.1.

Groves, G. V., 1972: Annual and semiannual zonal wind components and corresponding temperature and density variations, 60–130 km. *Planet. Space Sci.*, **20**, 2099–2112.

Hamilton, K. and J. D. Mahlman, 1988: General circulation model simulation of the semiannual oscillation in the tropical middle atmosphere. *J. Atmos. Sci.*, **45**, 3212–3235.

Harada, Y., H. Kamahori, C. Kobayashi, H. Endo, S. Kobayashi, Y. Ota, H. Onoda, K. Onogi, K. Miyaoka, and K. Takahashi, 2016: The JRA-55 reanalysis: Representation of atmospheric circulation and climate variability. *J. Meteor. Soc. Japan*, **94**, 269–302.

Hersbach, H., B. Bell, P. Berrisford, S. Hirahara, A. Horányi, J. Muñoz-Sabater, J. Nicolas, C. Peubey, R. Radu, D. Schepers, A. Simmons, C. Soci, S. Abdalla, X. Abellan, G. Balsamo, P. Bechtold, G. Biavati, J. Bidlot, M. Bonavita, G. De Chiara, P. Dahlgren, D. Dee, M. Diamantakis, R. Dragani, J. Flemming, R. Forbes, M. Fuentes, A. Geer, L. Haimberger, S.

Healy, R. J. Hogan, E. Hólm, M. Janisková, S. Keeley, P. Laloyaux, P. Lopez, C. Lupu, G. Radnoti, P. de Rosnay, I. Rozum, F. Vamborg, S. Villaume, and J.-N. Thépaut, 2020: The ERA5 global reanalysis. *Quart. J. Roy. Meteor. Soc.*, **146**, 1999–2049, doi: 10.1002/qj.3803.

Hitchman, M. H. and C. B. Leovy, 1986: Evolution of the zonal mean state in the equatorial middle atmosphere during October 1978 – May 1979. *J. Atmos. Sci*., **43**, 3159–3176.

Hirota, I., 1978: Equatorial waves in the upper stratosphere and mesosphere in relation to the semiannual oscillation of the zonal wind. *J. Atmos. Sci.*, **35**, 714–722.

Holton, J. R. and W. M. Wehrbein, 1980: A numerical model of the zonal mean circulation of the middle atmosphere. *Pure Appl. Geophys*., **118**, 284–306.

Iwao, K., and T., Hirooka, 2021: Opposite contributions of stationary and traveling planetary waves in the northern hemisphere winter middle atmosphere. *J. Geophys. Res. Atmos.,* **126**, e2020JD034195, doi:10.1029/2020JD034195.

Jackson, D. R. and L. J. Gray, 1994: Simulation of the semi-annual oscillation of the equatorial middle atmosphere using the Extended UGAMP General Circulation Model. *Q. J. Roy. Meteorol. Soc*., **120**, 1559–1588.

Kawatani, Y., T. Hirooka, K. Hamilton, A. K. Smith, and M. Fujiwara, 2020: Representation of the equatorial stratopause semiannual oscillation in global atmospheric reanalyses. *Atmos. Chem. Phys.*, **20**, 9115–9133, doi: 10.5194/acp-20-9115-2020.

Kishore Kumar, G., K. Kishore Kumar, W. Singer, C. Zülicke, S. Gurubaran, G. Baumgarten, G. Ramkumar, S. Sathishkumar, and M. Rapp, 2014: Mesosphere and lower thermosphere zonal wind over low latitudes: Relation to local stratospheric zonal winds and global circulation anomalies. *J. Geophys. Res. Atmos.* **119**, 10: 5913–5927, doi:10.1002/2014JD021610.

Kobayashi, S., Y. Ota, Y. Harada, A. Ebita, M. Moriya, H. Onoda, K. Onogi, H. Kamahori, C. Kobayashi, H. Endo, K. Miyaoka, and K. Takahashi, 2015: The JRA-55 reanalysis: General specifications and basic characteristics. *J. Meteor. Soc. Japan*, **93**, 5–48.

Kosaka Y., S. Kobayashi, Y. Harada, C. Kobayashi, H. Naoe, K. Yoshimoto, M. Harada, N. Goto, J. Chiba, K. Miyaoka, R. Sekiguchi, M. Deushi, H. Kamahori, T. Nakaegawa; T. Y.Tanaka, T. Tokuhiro, Y. Sato, Y. Matsushita, and K. Onogi, 2024: The JRA-3Q Reanalysis. *J. Meteor. Soc. Japan*, **102**, doi: 10.2151/jmsj.2024-004.

Koshin, D., K. Sato, K. Miyazaki, and S. Watanabe, 2020: An ensemble Kalman filter data assimilation system for the whole neutral atmosphere, *Geosci. Model Dev.*, **13**, 3145–3177, doi:10.5194/gmd-13-3145-2020.

Koshin, D., K. Sato, M. Kohma, and S. Watanabe, 2022: An update on the 4D-LETKF data assimilation system for the whole neutral atmosphere, *Geosci. Model Dev.*, **15**, 2293–2307, doi:10.5194/gmd-15-2293-2022.

Kumar, K. K., D. Swain, S. R. John, and G. Ramkumar, 2011: Simultaneous observations of SAO and QBO in winds, temperature and ozone in the tropical middle atmosphere over Thumba (8.5°N, 77°E). *Climate Dyn*., **37**, 1961–1973.

Livesey, N. J., W. G. Read, P. A. Wagner, L. Froidevaux, M. L. Santee, M. J. Schwartz, A. Lambert, L. F. Millán Valle, H. C. Pumphrey, G. L. Manney, R. A. Fuller, R. F. Jarnot, B. W. Knosp, R. R. Lay, 2022: Version 5.0x Level 2 and 3 data quality and description document, JPL D-105336 Rev. B, 177 pp. [Available online at https://mls.jpl.nasa.gov/data/v5-0_data_quality_document.pdf.]

Maeda, K., 1984: Semiannual oscillation of stratospheric ozone. *Geophys. Res. Lett.* **11**, 583-586.

Minobe, S., and T. Nakanowatari, 2002: Global structure of bidecadal precipitation variability in boreal winter. *Geophys. Res. Lett.*, **29**, 35-1–35-4.

Naoe, H. C. Kobayashi, S. Kobayashi, Y. Kosaka, and K. Shibata, 2025: Representation of quasi-biennial oscillation in JRA-3Q. *J. Meteor. Soc. Japan*. (accepted)

Onogi, K., J. Tsutsui, H. Koide, M. Sakamoto, S. Kobayashi, H. Hatsushika, T. Matsumoto, N. Yamazaki, H. Kamahori, K. Takahashi, S. Kadokura, K. Wada, K. Kato, R. Oyama, T. Ose, N. Mannoji, and R. Taira, 2007: The JRA-25 reanalysis. *J. Meteor. Soc. Japan*, **85**, 369–432.

Randel, W. J., 1987: The evaluation of wind from geopotential height data in the stratosphere. *J. Atmos. Sci.*, **44**, 3097–3120.

Randel, W., P. Udelhofen, E. Fleming, M. Geller, M. Gelman, K. Hamilton, D. Karoly, D. Ortland, S. Pawson, R. Swinbank, F. Wu, M. Baldwin, M.-L. Chanin, P. Keckhut, K. Labitzke, E. Remsberg, A. Simmons, and D. L. Wu, 2004: The SPARC intercomparison of middle-atmosphere climatologies. *J. Climate,* **17**, 986–1003.

Ray, E. A., J. R. Holton, E. F. Fishbein, L. Froidevaux, and J. W. Waters, 1994: The tropical semiannual oscillations in temperature and ozone as observed by the MLS, *J. Geophys. Res.,* **51***,* 3045-3052, doi:10.1175/1520-0469(1994)051<3045:TTSOIT>2.0.CO;2.

Ray, E. A., M. J. Alexander, and J. R. Holton, 1998: An analysis of the structure and forcing of the equatorial semiannual oscillation in zonal wind, *J. Geophys. Res.,* **103**, 1759–1774, doi:10.1029/97JD02679.

Reed, R. J., 1966: Zonal wind behavior in the equatorial stratosphere and lower mesosphere, *J. Geophys. Res.*, **71**, 4223–4233.

Sen, P. K., 1968: Estimates of the regression coefficient based on Kendall's tau. *J. Amer. Stat. Assoc*., **63**, 1379–1389.

Siegel, A. F., 1982: Robust regression using repeated medians. *Biometrika*, **69**, 242–244.

Smith, A. K., R. R. Garcia, A. C. Moss, and N. J. Mitchell, 2017: The semiannual oscillation of the tropical zonal wind in the middle atmosphere derived from satellite geopotential height retrievals. *J. Atmos. Sci.*, **74**, 2413–2425, doi:10.1175/JAS-D-17-0067.1.

Smith, A. K., L. A. Holt, R. R. Garcia, J. A. Anstey, F. Serva, N. Butchart, S. Osprey, A. C. Bushell, Y. Kawatani, Y., Y.-H. Kim, F. Lott, P. Braesicke, C. Cagnazzo, C.-C. Chen, H.-Y. Chun, L. Gray, T. Kerzenmacher, N. Naoe, J. Richter, S. Versick, V. Schenzinger, S. Watanabe, and K. Yoshida, 2020: The equatorial stratospheric semiannual oscillation and time-mean winds in QBOi models. Q. *J. Roy. Meteor. Soc.*, 1–17, **148**, doi:10.1002/qj.3690.

SPARC, 2002: Temperature and Zonal Wind Climatology, SPARC Data Centre [data set]. [Available at: ftp://sparc-ftp1.ceda.ac.uk/sparc/ref_clim/randel/temp_wind/] (last access: 12 February 2024).

SPARC, 2022: *SPARC Reanalysis Intercomparison Project (S-RIP) Final Report. M.* Fujiwara, G. L., Manney, L. J. Gray, and J. S. Wright (Eds.), SPARC Report No. 10, WCRP-17/2020, 612pp. doi: 10.17874/800dee57d13. [Available online at www.sparc-climate.org/publications/sparc-reports.]

Shibata, K. and M. Deushi, 2012: Future changes in the quasi-biennial oscillation under a greenhouse gas increase and ozone recovery in transient simulations by a chemistry-climate model. Greenhouse Gases - Emission, Measurement and Management, Dr. Guoxiang Liu (Ed.), 355-386, ISBN: 978-953-51-0323-3, InTech.

Shibata, K., and H. Naoe, 2022: Decadal amplitude modulations of the stratospheric quasi-biennial oscillation. *J. Meteor. Soc. Japan*, **100**, 29–44, doi:10.2151/jmsj.2022-001.

Shibata, K., 2022: Studies of the effect of seasonal cycle on the equatorial quasi-biennial oscillation with a chemistry-climate model. *Climate*, **10**, 99, doi:10.3390/cli10070099.

Torrence, C., and G. P. Compo, 1998: A practical guide to wavelet analysis. *Bull. Amer. Meteor. Soc.*, **79**, 61–78.

Uppala, S. M., P. W. Kållberg, A. J. Simmons, U. Andrae, V. da Costa Bechtold, M. Fiorino, J. K. Gibson, J. Haseler, A. Hernandez, G. A. Kelly, X. Li, K. Onogi, S. Saarinen, N. Sokka, R. P. Allan, E. Andersson, K. Arpe, M. A. Balmaseda, A. C. M. Beljaars, L. van de Berg, J. Bidlot, N. Bormann, S. Caires, F. Chevallier, A. Dethof, M. Dragosavac, M. Fisher, M. Fuentes, S. Hagemann, E. Hólm, B. J. Hoskins, L. Isaksen, P. A. E. M. Janssen, R. Jenne, A. P. Mcnally, J.-F. Mahfouf, J.-J. Morcrette, N. A. Rayner, R. W. Saunders, P. Simon, A. Sterl, K. E. Trenberth, A. Untch, D. Vasiljevic, P. Viterbo, and J. Woollen, 2005: The ERA-40 reanalysis. *Quart. J. Roy. Meteor. Soc.,* **131**, 2961–3012.

Figure legends

Fig. 1. Latitude-height cross sections of the SAO amplitudes of the MLS (a) zonal wind, (b) temperature, SABER (c) zonal wind, and (d) temperature from 10 to 0.005 hPa between 30°S and 30°N. Contour interval is 5 m s^{-1} for wind, and 1 K for temperature.

Fig. 2. Latitude-height cross sections of the ANN amplitudes of the MLS (a) zonal wind, (b) temperature, SABER (c) zonal wind, and (d) temperature from 10 to 0.01 hPa between 30°S and 30°N. Contour interval is 10 m s^{-1} for zonal wind, and 1 K for temperature.

Fig. 3. Month-latitude cross sections of the climatological unfiltered zonal wind of the MLS (a) at 0.01 hPa, (b) at 1 hPa, SABER (c) at 0.01 hPa, and (d) at 1 hPa between 30°S and 30°N. Contour interval is 10 m s^{-1}. Climatological annual mean is subtracted at each latitude.

Fig. 4. Month-latitude cross sections of the climatological ANN zonal wind of the MLS (a) at 0.01 hPa, (b) at 1 hPa, SABER (c) at 0.01 hPa, and (d) at 1 hPa between 30°S and 30°N. Contour interval is 5 m s^{-1}.

Fig. 5. Month-latitude cross sections of the SAO zonal wind of MLS (a) at 0.01 hPa, (b) at 1 hPa, SABER (c) at 0.01 hPa, and (d) at 1 hPa between 30°S and 30°N. Contour interval is 5 m s^{-1}.

Fig. 6. Month-height cross sections of the MLS (a) unfiltered zonal wind, (b) ANN zonal wind, (c) SAO zonal wind, SABER (d) unfiltered zonal wind, (e) ANN zonal wind, and (f) SAO zonal wind, averaged between 10°S and 10°N, from 10 to 0.01 hPa. Contour interval is 5 m s^{-1}.

Fig. 7. Seasonal cycles of the MLS (thin lines) and SABER (thick lines) zonal wind of (a) the MSAO at 0.01 hPa and (b) the SSAO at 1 hPa. Dots represent monthly values of MLS and solid lines display cubic spline fits.

Fig. 8. Latitude-height cross sections of the SAO amplitudes of the JRA-3Q (a) zonal wind, (b) temperature, ERA5 (c) zonal wind, (d) temperature, MERRA-2 (e) zonal wind, and (f) temperature. Contour intervals are 5 m s^{-1} for wind and 1 K for temperature.

Fig. 9. Month-latitude cross sections of the SAO zonal wind of JRA-3Q (a) at 0.01 hPa, and (b) at 1 hPa, ERA5 (c) at 0.01 hPa, (d) at 1 hPa, MERRA-2 (e) at 0.0 1hPa, and (f) at 1 hPa between 30°S and 30°N. Contour interval is 5 m s^{-1}.

Fig. 10. Month-height cross sections of the SAO zonal wind of (a) JRA-3Q, (b) ERA5, and (c) MERRA-2 from 10 to 0.01 hPa. The SAO zonal wind is averaged between 10°S and 10°N. Contour interval is 5 m s^{-1}.

Fig. 11. Time series of the SAO amplitude of the MLS (a) zonal wind, (b) temperature, SABER (c) zonal wind, and (d) temperature from 10 to 0.01 hPa. The amplitudes are for the wind and temperature averaged between 10°S and 10°N. Contour interval is 10 m s^{-1} for wind and 5 K for temperature.

Fig. 12. Vertical profiles of the linear trends of the SAO amplitudes of the SABER and MLS (a) zonal wind and (b) temperature. The amplitude is for the wind and temperature, averaged between 10°S and 10°N. Unit of the trend is m s^{-1} $(\text{decade})^{-1}$ for wind and K $(\text{decade})^{-1}$ for temperature. Red crosses, blue squares, and green circles represent statistical significance higher than the 99%, 95%, and 90% levels, respectively.

Fig. 13. Vertical profiles of the linear trends of the SAO amplitudes of the JRA-3Q, ERA5, and MERRA-2 (a) zonal wind and (b) temperature, averaged between 10°S and 10°N. Unit of the trend is m s^{-1} $(\text{decade})^{-1}$ for wind and K $(\text{decade})^{-1}$ for temperature. Red crosses, blue squares, and

green circles represent statistical significance higher than the 99%, 95%, and 90% levels, respectively.

Fig. 14. Lag-height cross section of the lagged correlation coefficient of the detrended SAO amplitudes of the MLS (a) zonal wind, (b) temperature, SABER (c) zonal wind, and (d) temperature between a reference altitude and other altitudes. The reference altitude is 1 hPa for zonal wind and 2 hPa for temperature. The amplitudes are calculated from zonal wind and temperature averaged between 10°S and 10°N. The abscissa is time-lag in months. Contour interval is 0.2, and color shading represents statistical significance higher than the 95% level.

Fig. 15. Lag-height cross section of the lagged correlation coefficient of the detrended SAO amplitudes of the JRA-3Q (a) zonal wind, (b) temperature, ERA5 (c) zonal wind, (d) temperature, MERRA-2 (e) zonal wind, and (f) temperature between a reference altitude and other altitudes. The reference altitude is 1 hPa for zonal wind and 2 hPa for temperature. The amplitudes are calculated from zonal wind and temperature averaged between 10°S and 10°N. The abscissa is time-lag in months. Contour interval is 0.2, and color shading represents statistical significance higher than the 95% level.

Fig. 16. Time-period cross section of the amplitudes over the periods from 3 to 15 months for the JRA-3Q (a) zonal wind, (b) temperature, ERA5 (b) zonal wind, (c) temperature, MERRA-2 (d) zonal wind, and (e) temperature. The amplitudes are calculated from zonal wind at 1 hPa and temperature at 2 hPa averaged between 10°S and 10°N.

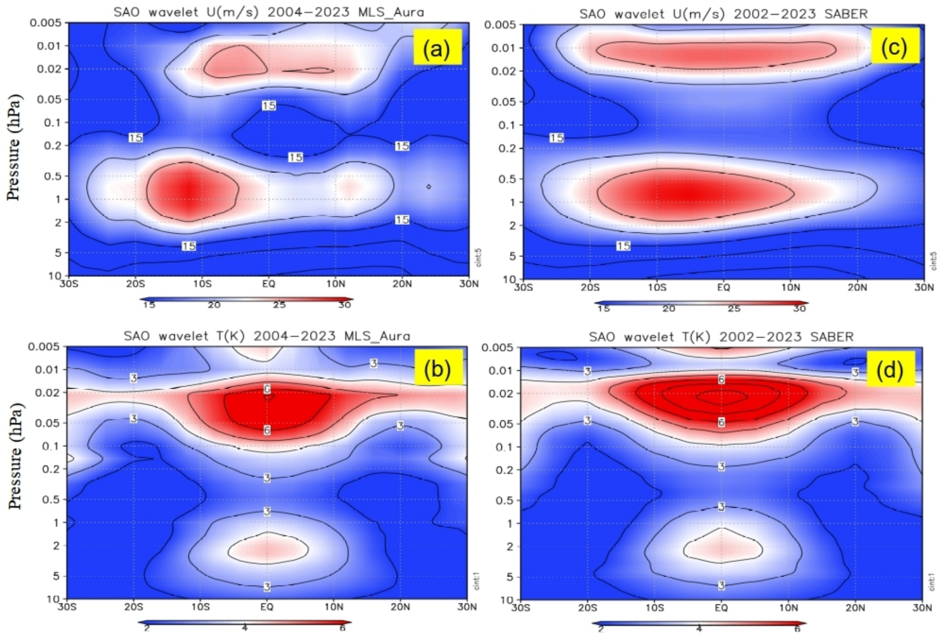

Fig. 1. Latitude-height cross sections of the SAO amplitudes of the MLS (a) zonal wind, (b) temperature, SABER (c) zonal wind, and (d) temperature from 10 to 0.005 hPa between 30°S and 30°N. Contour interval is 5 $m s^{-1}$ for wind, and 1 K for temperature.

279x210mm (96 x 96 DPI)

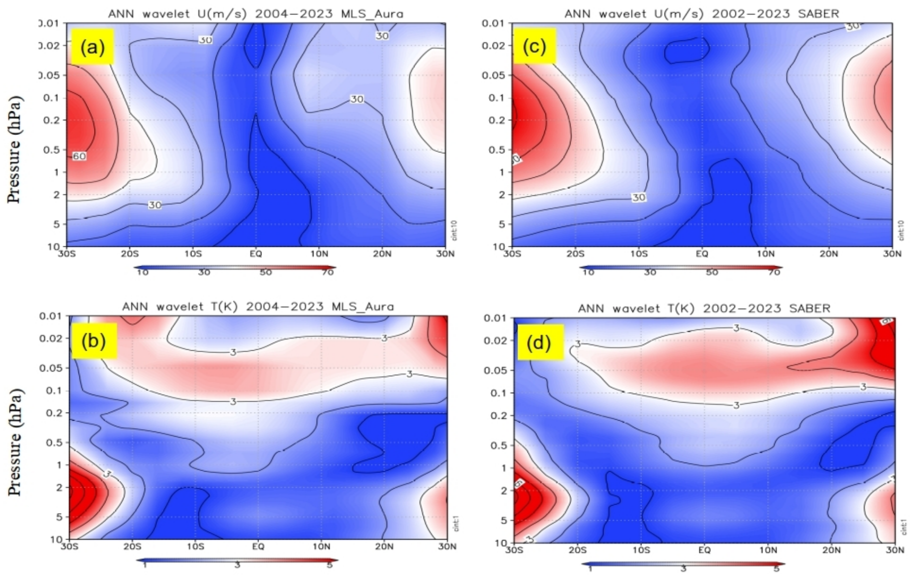

Fig. 2. Latitude-height cross sections of the ANN amplitude of the MLS (a) zonal wind, (b) temperature, SABER (c) zonal wind, (d) temperature from 10 to 0.01 hPa between 30°S and 30°N. Contour interval is 10 m s^{-1} for wind, and 1 K for temperature.

279x210mm (96 x 96 DPI)

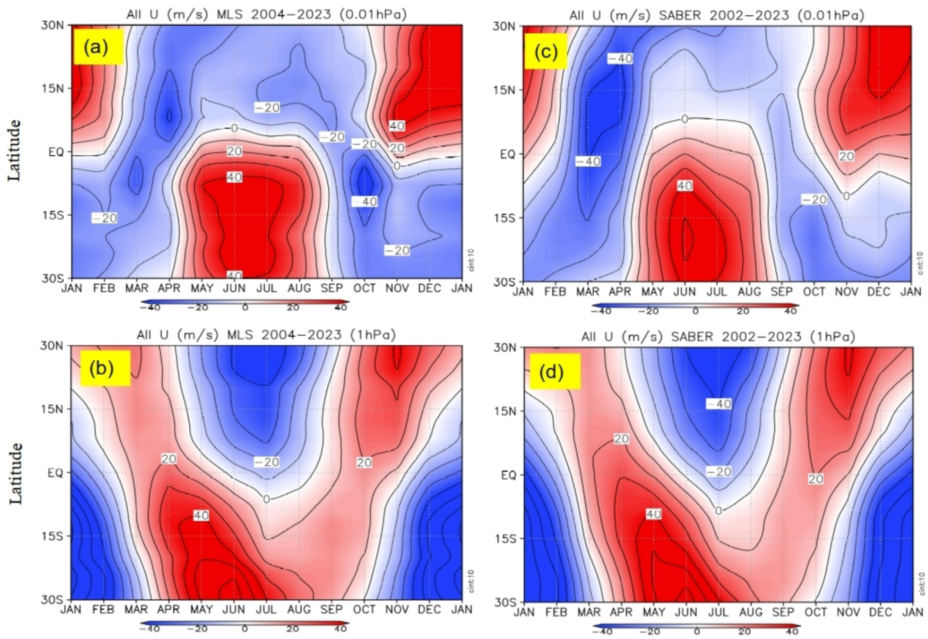

Fig. 3. Month-latitude cross sections of the climatological unfiltered zonal wind of MLS (a) at 0.01 hPa, (b) at 1 hPa, SABER (c) at 0.01 hPa, and (d) at 1 hPa between 30°S and 30°N. Contour interval is 10 ms^{-1}. Climatological annual mean is subtracted at each latitude.

279x210mm (96 x 96 DPI)

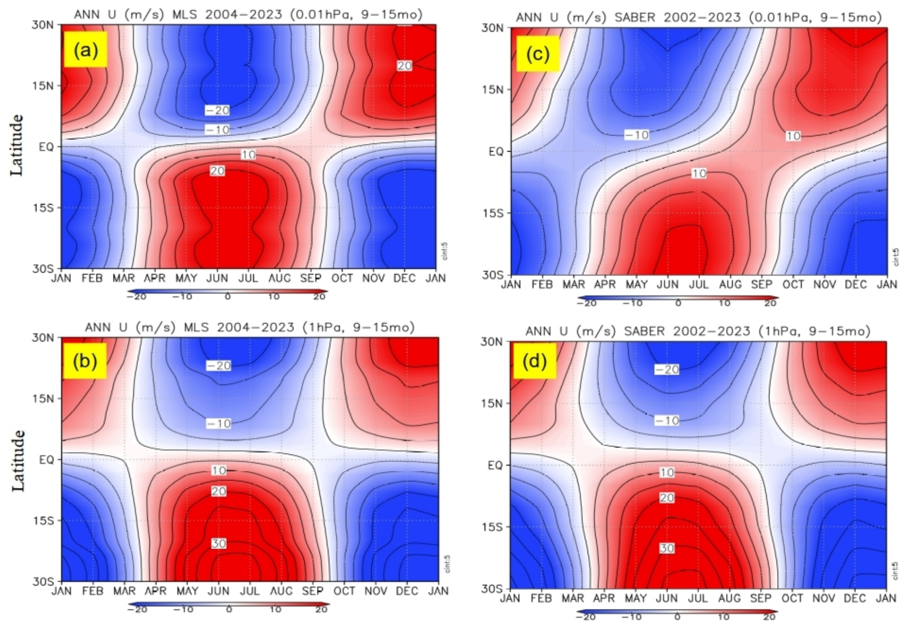

Fig. 4. Month-latitude cross sections of the climatological ANN zonal wind of MLS (a) at 0.01 hPa, (b) at 1 hPa, SABER (c) at 0.0 1hPa, and (d) at 1 hPa between 30°S and 30°N. Contour interval is 5 ms^{-1}.

279x210mm (96 x 96 DPI)

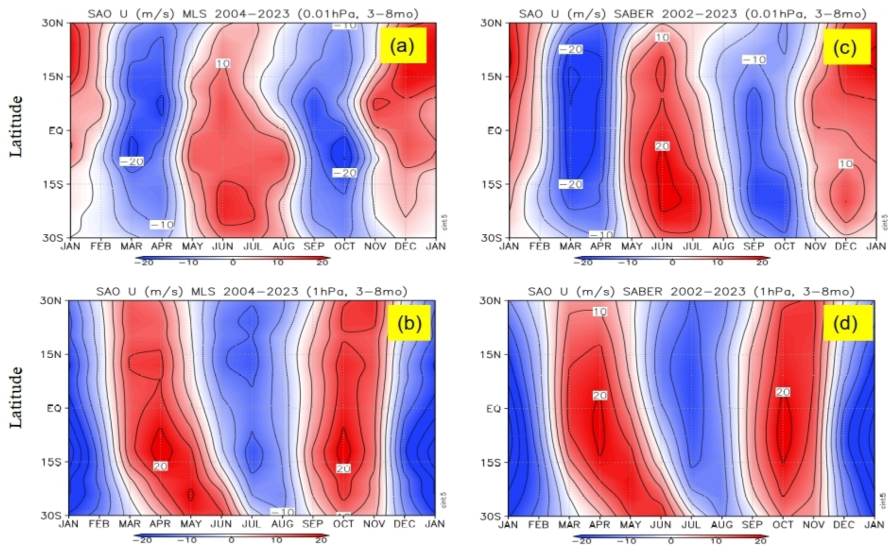

Fig. 5. Month-latitude cross sections of the SAO zonal wind of MLS (a) at 0.01 hPa, (b) at 1 hPa, SABER (c) at 0.01 hPa, and (d) at 1 hPa between 30°S and 30°N. Contour interval is 5 m s^{-1}.

279x210mm (96 x 96 DPI)

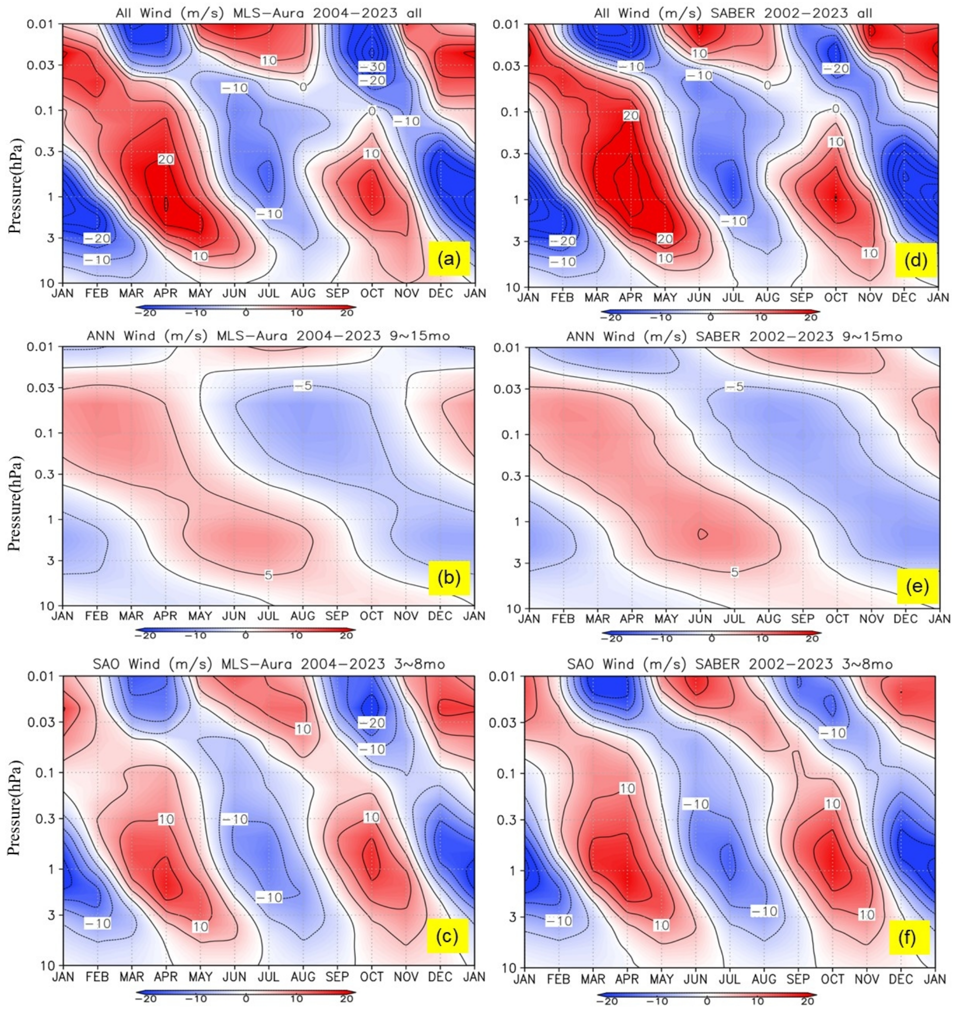

Fig. 6. Month-height cross sections of the MLS (a) unfiltered zonal wind, (b) ANN zonal wind, (c) SAO zonal wind, SABER (d) unfiltered zonal wind, (e) ANN zonal wind, and (f) SAO zonal wind, averaged between 10°S and 10°N, from 10 to 0.01 hPa. Contour interval is 5 m s^{-1}.

339x400mm (96 x 96 DPI)

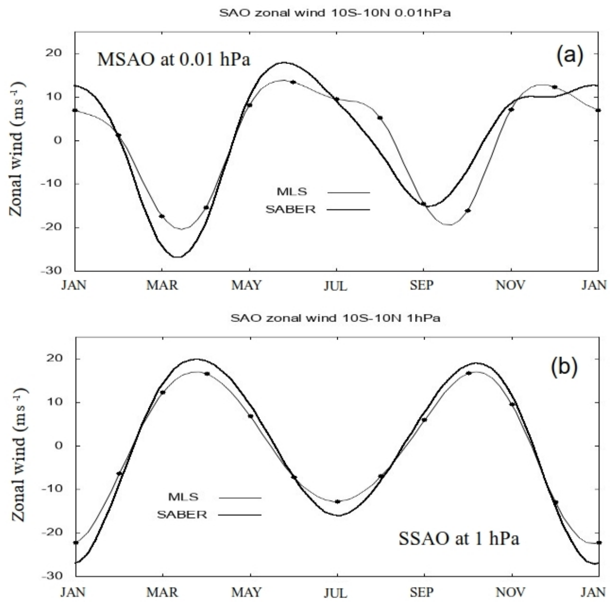

Fig. 7. The seasonal cycles of the MLS (thin) and SABER (thick) zonal wind of (a) the MSAO at 0.01 hPa and (b) the SSAO at 1 hPa. Dots represent monthly values of MLS and solid lines display cubic spline fits.

279x210mm (96 x 96 DPI)

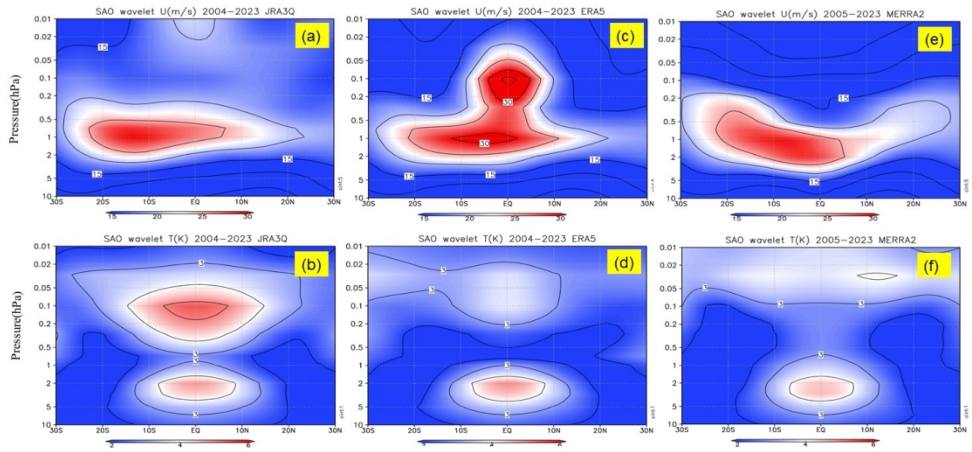

Fig. 8. Latitude-height cross sections of the SAO amplitudes of the JRA-3Q (a) zonal wind, (b) temperature, ERA5 (c) zonal wind, (d) temperature, MERRA2 (e) zonal wind, and (f) temperature. Contour intervals are 5 m s^{-1} for zonal wind and 1K for temperature.

400x225mm (96 x 96 DPI)

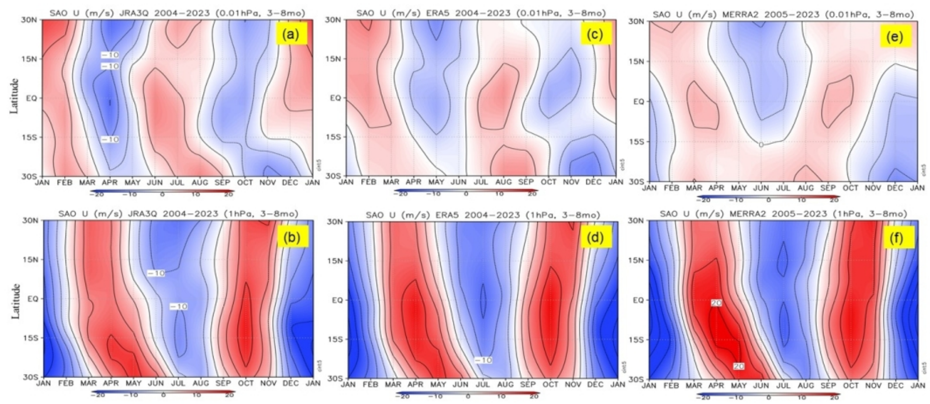

Fig. 9. Month-latitude cross sections of the SAO zonal wind of JRA-3Q (a) at 0.01 hPa, (b) at 1 hPa, ERA5 (c) at 0.01 hPa, (d) at 1 hPa, MERRA-2 (e) at 0.0 1hPa, and (f) at 1 hPa between 30° S and 30° N. Contour interval is 5 m s^{-1}.

410x250mm (96 x 96 DPI)

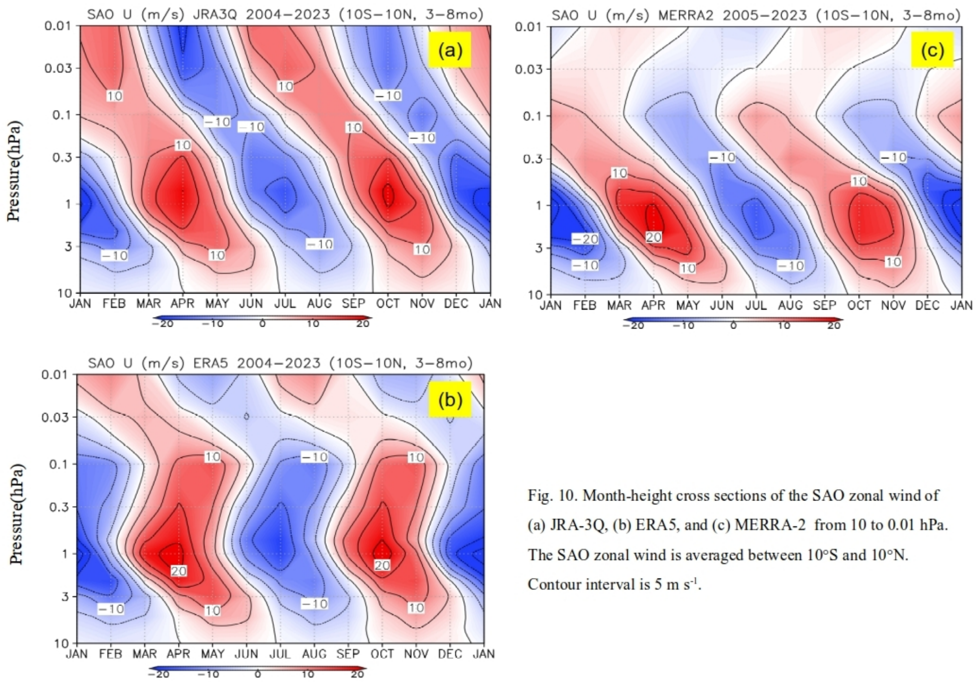

Fig. 10. Month-height cross sections of the SAO zonal wind of (a) JRA-3Q, (b) ERA5, and (c) MERRA-2 from 10 to 0.01 hPa. The SAO zonal wind is averaged between 10°S and 10°N. Contour interval is 5 m s^{-1}.

279x210mm (96 x 96 DPI)

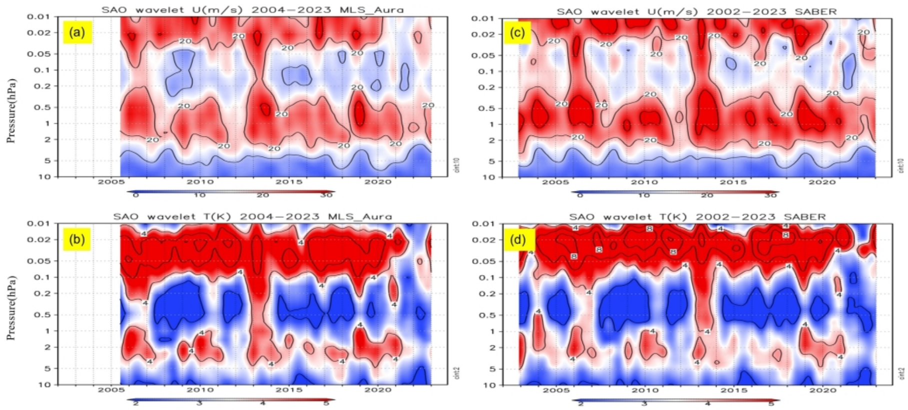

Fig. 11. Time series of the SAO amplitude of the MLS (a) zonal wind, (b) temperature, SABER (c) zonal wind, and (d) temperature from 10 to 0.01 hPa. The amplitudes are for wind and temperature averaged between 10° S and 10° N. Contour interval is 10 m s^{-1} for wind and 5 K for temperature.

950x460mm (96 x 96 DPI)

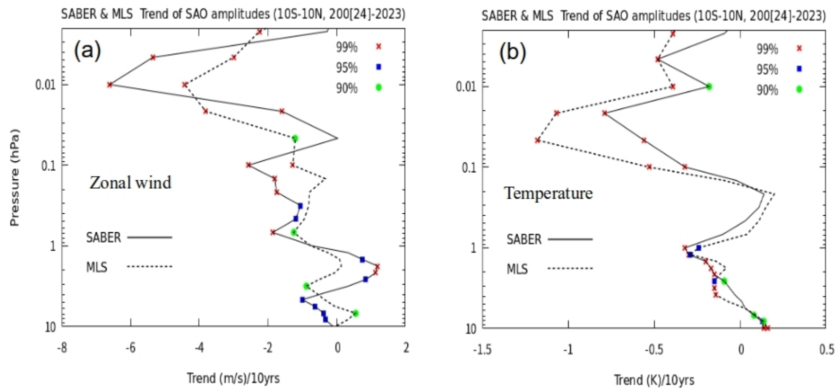

Fig. 12. Vertical profiles of the linear trends of the SAO amplitude of the SABER and MLS (a) zonal wind and (b) temperature averaged between 10°S and 10°N. Unit of the trend is m s^{-1} $(decade)^{-1}$ for wind and K $(decade)^{-1}$ for temperature. Red crosses, blue squares, and green circles represent statistical significance higher than the 99%, 95% , and 90% levels, respectively.

279x210mm (96 x 96 DPI)

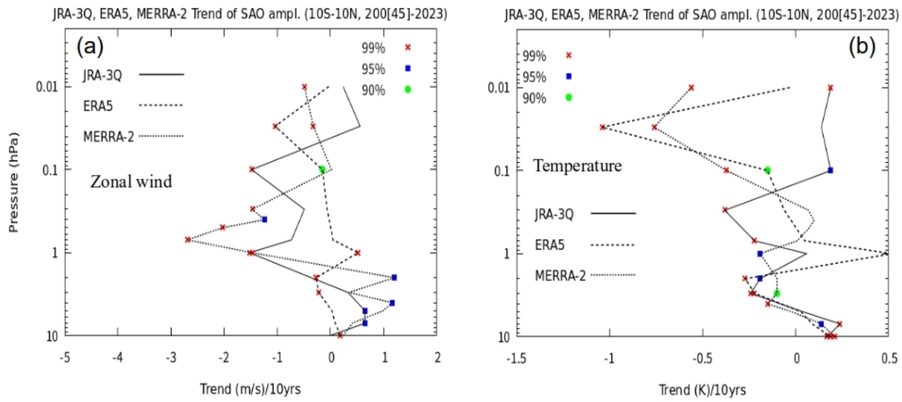

Fig. 13. Vertical profiles of the linear trends of the SAO amplitudes of the JRA-3Q, ERA5, and MERRA-2 (a) zonal wind and (b) temperature, averaged between 10°S and 10°N. Unit of the trend is m s^{-1} $(decade)^{-1}$ for wind and K $(decade)^{-1}$ for temperature. Red crosses, blue squares, and green circles represent statistical significance higher than the 99%, 95%, and 90% levels, respectively.

279x210mm (96 x 96 DPI)

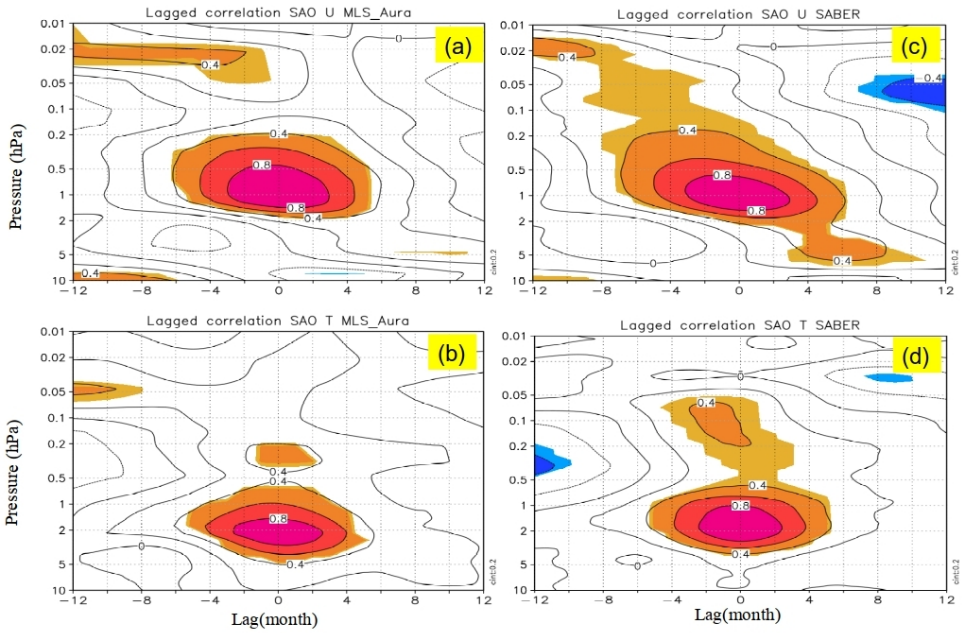

Fig. 14. Lag-height cross section of the lagged correlation coefficient of the detrended SAO amplitudes of the MLS (a) zonal wind, (b) temperature, SABER (c) zonal wind, and (d) temperature between a reference altitude and other altitudes. The reference altitude is 1 hPa for wind and 2 hPa for temperature. The amplitudes are calculated from zonal wind and temperature averaged between 10°S and 10°N. The abscissa is time-lag in months. Contour interval is 0.2, and color shading represents statistical significance higher than the 95% level.

279x210mm (96 x 96 DPI)

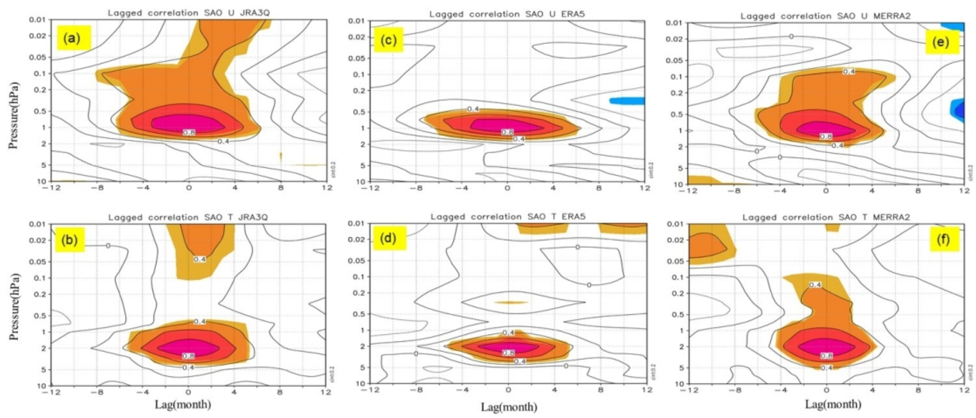

Fig. 15. Lag-height cross section of the lagged correlation coefficient of the detrended SAO amplitudes of the JRA-3Q (a) zonal wind, (b) temperature, ERA5 (c) zonal wind, (d) temperature, MERRA-2 (e) zonal wind, and (f) temperature between a reference altitude and other altitudes. The reference altitude is 1 hPa for wind and 2 hPa for temperature. The amplitudes are calculated from zonal wind and temperature averaged between 10° S and 10° N. The abscissa is time-lag in months. Contour interval is 0.2, and color shading represents statistical significance higher than the 95% level.

408x220mm (96 x 96 DPI)

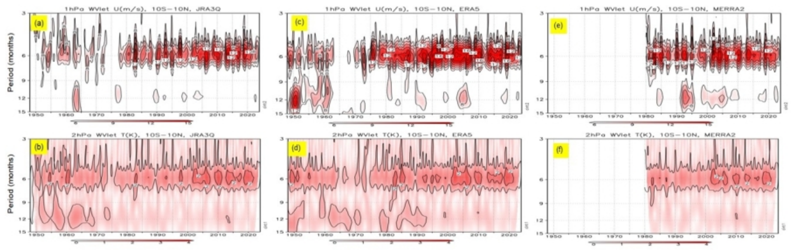

Fig. 16. Time-period cross section of the amplitudes over the periods from 3 to 15 months for the JRA-3Q (a) zonal wind, (b) temperature, ERA5 (c) zonal wind, (d) temperature, MERRA-2 (e) zonal wind, and (f) temperature. The amplitudes are calculated from zonal wind at 1 hPa and temperature at 2 hPa averaged between 10°S and 10°N.

451x300mm (96 x 96 DPI)